Are the Fe-rich-clay veins in the igneous rock of the Kansas (USA) Precambrian crust of magmatic origin?

Valentine Combaudon, Olivier Sissmann, Sylvain Bernard, Jean-Christophe Viennet, Valentine Megevand, Corentin Le Guillou, Julia Guélard, Isabelle Martinez, François Guyot, Hannelore Derluyn, et al.

To cite this version:

Valentine Combaudon, Olivier Sissmann, Sylvain Bernard, Jean-Christophe Viennet, Valentine Megevand, et al.. Are the Fe-rich-clay veins in the igneous rock of the Kansas (USA) Precambrian crust of magmatic origin?. Lithos, 2024, 474-475, pp.107583. ⟨10.1016/j.lithos.2024.107583⟩. ⟨hal-04533762⟩

Are the Fe-rich-clay veins in the igneous rock of the Kansas (USA) Precambrian crust of magmatic origin?

Valentine Combaudon*[1,2], Olivier Sissmann[1], Sylvain Bernard[3], Jean-Christophe Viennet[3], Valentine Megevand[3,4], Corentin Le Guillou[5], Julia Guélard[1], Isabelle Martinez[6], François Guyot[3], Hannelore Derluyn[2] and Eric Deville[1]

1: IFPEN, Rueil-Malmaison, France ; 2: Université de Pau et des Pays de l'Adour, E2S UPPA, CNRS, LFCR, Pau, France; 3: Muséum National d'Histoire Naturelle, Sorbonne Université, CNRS UMR 7590, Institut de Minéralogie, Physique des Matériaux et Cosmochimie, 75005, Paris, France ; 4: Département des Sciences de la Terre, Ecole Normale Supérieure de Lyon, France ; 5: Université Lille, CNRS, INRA, ENSCL, UMR 8207, UMET, Unité Matériaux et Transformations, 59000 Lille, France 1 ; 6: Université de Paris Cité, Institut de Physique du Globe de Paris, CNRS, 75005, Paris, France

* Corresponding author: combaudon.valentine@gmail.com – Avenue de l'Université, 64000, Pau (France)

Highlights

- The igneous rock from the Kansas basement is a fayalite-bearing monzo-diorite.
- Two generations of iron-rich clay minerals are described within the monzo-diorite.
- Reduced-iron-rich clay minerals are formed by precipitation of a late magmatic fluid.
- Oxidized-iron-rich clay minerals are formed by deuteric alteration of the fayalite.
- Late magmatic alteration could be prone to produce hydrogen by iron oxidation.

Abstract

The North American Mid-Continent rift (MCR) is a 1.1 Ga aborted rift, which has recently become an area of intense focus for energy resource exploration following the report of H_2 emissions. To document the nature of the producing rocks, we conducted a multi-scale study on preserved drill-core samples from the DR1-A well located in the same area as the H_2-producing wells in Kansas. We showed that this well reaches an unmapped part of the MRS composed of fayalite-bearing monzo-diorites in which we identified atypical veins of iddingsite, a complex mixing of Fe-rich phyllosilicates. Combining scanning and transmission electron microscopy (SEM and TEM) with scanning transmission X-ray microscopy (STXM) allowed us to differentiate at least two types of sub-micro-meter Fe-rich veins. A central reduced vein cutting the fayalite, other mafic minerals , the plagioclase, and to a lesser extent the alkali feldspar, contains a complex mix of serpentine, chlorite, and mica. Furthermore, a border vein, with a higher degree of Fe-oxidation, is found to be contained only within the fayalite. This external vein mainly contains iron and silicon, together with a few percent of potassium and calcium, and can be divided into two sub-veins composed of Fe^{3+}-rich interstratified chlorite-smectite and Fe^{3+}-rich serpentine in direct contact with the fayalite.

Textures and microstructures of these phyllosilicates suggest that they have crystallized from a late magmatic and differentiated fluid, which precipitation produced the central vein together with the exsolution of an H_2O-enriched fluid phase. This exsolved fluid, chemically far from equilibrium with the fayalite, appears to have induced a deuteric alteration of the fayalite, leading to the crystallization of the external veins enriched in ferric iron. These observations bring new perspectives on the history of formation of iron-rich clay minerals, which may, somehow, be related to H_2 production.

Keywords: fayalite, iron-rich clays, Mid-Continent rift, Precambrian, hydrogen

1. Introduction

Since the eighties, old water wells in northeastern Kansas have been emitting gas with an average of 29-37 mol% of natural hydrogen (Coveney et al., 1987). A more recent study from Guélard and co-authors (2017) shows similar gas composition up to 92 mol% of H_2, highlighting a persistent regional flux. Noble gas analyses and on-site spectrophotometry on water samples showed that the gas flux coming from the wells has a deep crustal origin associated with iron oxidation, coinciding with these wells reaching the basement (Guélard et al., 2017). The basement in the area corresponds to the Mid-Continent rift (MCR), a 1.1 Ga aborted rift composed of a km-scale accumulation of mafic rocks intruded in the Precambrian granitoid crust (Woelk et al., 1991). The emplacement of the rift was responsible for a major crustal reworking, resulting in half grabens bounded by normal faults (Ojakangas et al., 2011). The last tectonic event occurred during the Pennsylvanian (300 million years ago) and was responsible for reactivating the normal Proterozoic faults in crustal faults and for uplifting major parts of the basement (Merriam., 1963; Coveney et al., 1987; Newell et al., 2007). The H_2-emitting wells are located above the Nemaha High and the Humboldt crustal fault, in northeastern Kansas, and are also located about tens of kilometers east of the mapped area of the Mid-Continent rift (Figure 1). The source of hydrogen emissions has thus been attributed, thanks to previous gas analyses, to the Precambrian crust and potentially to the MCR (Guélard et al., 2017). Yet, the fine-scale petrography of the producing rocks has remained poorly documented.

Here, we report the characterization of preserved drill-core samples coming from the DR1-A well located above the Nemaha High and the Humboldt fault and reaching the basement (Figure 1). It crosses 350 meters of Paleozoic sedimentary rocks and nearly 100 meters of Precambrian basement rocks (Figure 1). We report here the results of a multi-scale petrographic study including scanning electron microscopy (SEM), scanning transmission X-ray microscopy coupled to X-ray absorption near edge structure spectroscopy (STXM-XANES), and transmission electron microscopy (TEM) performed on two samples K1 and K2 from the DR1-A well. This study, thus, describes the mineralogy of the rocks investigated and the petrological processes having led to the production of the late phases based on the fine scale partitioning of iron, elemental composition, and textural and structural specificities.

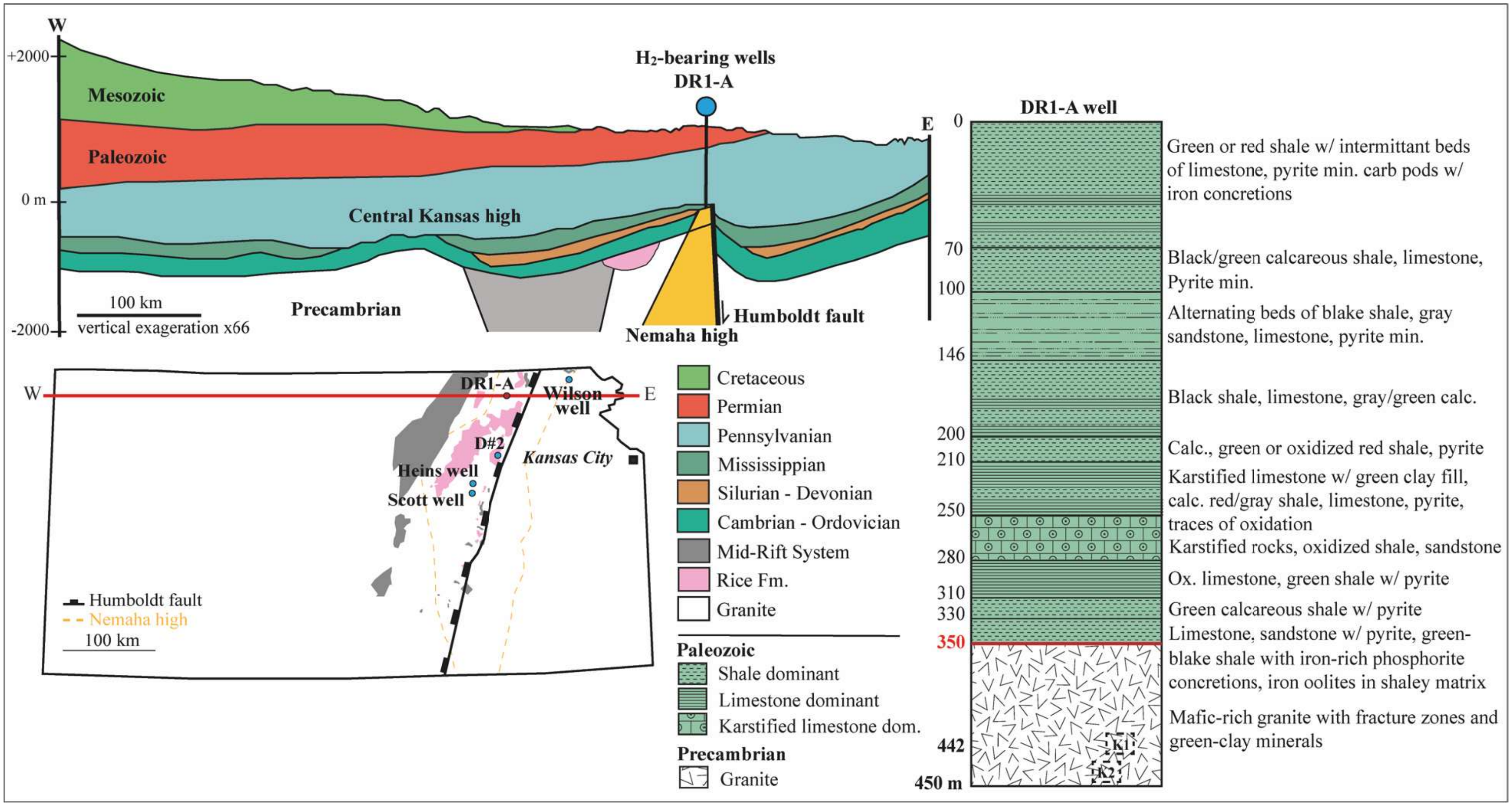
W
+2000
0 m
-2000
Mesozoic
Paleozoic
Central Kansas high
Precambrian
100 km
vertical exageration x66
H_2-bearing wells
DR1-A
E
Humboldt fault
Nemaha high
W
E
DR1-A
Wilson well
D#2
Kansas City
Heins well
Scott well
Humboldt fault
Nemaha high
100 km
Cretaceous
Permian
Pennsylvanian
Mississippian
Silurian - Devonian
Cambrian - Ordovician
Mid-Rift System
Rice Fm.
Granite
Paleozoic
Shale dominant
Limestone dominant
Karstified limestone dom.
Precambrian
Granite
DR1-A well
0
70
100
146
200
210
250
280
310
330
350
442
450 m
K1
K2
Green or red shale w/ intermittant beds of limestone, pyrite min. carb pods w/ iron concretions
Black/green calcareous shale, limestone, Pyrite min.
Alternating beds of blake shale, gray sandstone, limestone, pyrite min.
Black shale, limestone, gray/green calc.
Calc., green or oxidized red shale, pyrite
Karstified limestone w/ green clay fill, calc. red/gray shale, limestone, pyrite, traces of oxidation
Karstified rocks, oxidized shale, sandstone
Ox. limestone, green shale w/ pyrite
Green calcareous shale w/ pyrite
Limestone, sandstone w/ pyrite, green-blake shale with iron-rich phosphorite concretions, iron oolites in shaley matrix
Mafic-rich granite with fracture zones and green-clay minerals

Figure 1: West-East cross-section of Kansas with the location of the H_2-bearing wells and the DR1-A well (modified from Bickford et al., 1981, Kansas Geological Survey (1984), Coveney et al., 1987, and Guélard et al., 2017), simplified geological map of the basement top with the location of the H_2-bearing wells and DR1-A well (modified from Bickford et al., 1981, Coveney et al., 1987 and Guélard et al., 2017) and schematic stratigraphic log of the DR1-A well with the position of K1 and K2 samples (descriptions of the Paleozoic units are from the DR1-A drilling well report and are summary of the rock description's provided in the report. For more details, please refer to the drilling report available on the Kansas Geological Survey website).

2. Materials and methods

2.1. Samples

The K1 and K2 samples belong to the DR1-A well (Figure 1). The depth of the well is 457 meters. K1 sample corresponds to a depth of 442 meters while K2 sample corresponds to a depth of 450 meters. The preserved drill-core samples were provided by the Kansas Geological Survey (KGS).

2.2. Mineralogy

Optical microscopy images have been acquired with a petrographic microscope at Institut Français du Pétrole et des Energies Nouvelles (IFPEN, Rueil-Malmaison, France) in transmitted and reflected light. Scanning Electron Microscopy (SEM) and Energy-dispersive X-ray spectroscopy (EDS) mapping were performed on thin sections of the K1 and K2 samples using a Zeiss Gemini SEM at IFPEN (Rueil-Malmaison, France) and a Tescan VEGAIL LSU SEM at Muséum National d'Histoire Naturelle (Paris, France). International MAC standards for olivine, forsterite, diopside, albite and orthoclase were used to calibrate the acquired signal. The SEM chemical compositions of the standards were also compared to their chemical compositions acquired with a microprobe. Images and chemical analyses were performed at a 15 kV accelerating voltage using an 8 mm working distance in backscattered electron detection mode. Data were processed using the Hyperspy software (de la Peña et al. 2017).

2.3. FIB

To be characterized by STXM-XANES and TEM, samples must be transparent to electrons, i.e., with a thickness between 30 to 80 nm. To obtain electron-transparent sections, the samples were prepared using an SEM equipped with a Focused Ion Beam (FIB). This technique allowed us to prepare nanometric-scale samples that were studied to obtain high-resolution information (Ciobanu et al., 2011). FIB-thin sections were extracted from the K1 and K2 samples using an FEI Strata DB 235 (IEMN, Lille, France) at low Ga-ion current to minimize local gallium implantation, amorphization, mixing of components, local compositional changes, or redeposition of the sputtered material on the sample surface (Bernard et al., 2009; Wirth, 2009).

2.4. Scanning transmission X-ray microscopy and X-ray absorption near edge structure spectroscopy

Scanning transmission X-ray microscopy (STXM) and X-ray absorption near edge structure (XANES) data were collected on the FIB-thin sections using the HERMES STXM beamline at the synchrotron SOLEIL (Belkhou et al., 2015; Swaraj et al., 2017). XANES combined with STXM enables the speciation of a chemical element (iron in this work), obtained in the form of an absorption spectrum, and the quantification of the element of interest, represented as a chemical map of the FIB-thin section (Bourdelle et al., 2013). XANES data were extracted from image stacks collected at energy increments of 0.1 eV over the iron (690–740 eV) absorption range with a dwell time of 1 ms per pixel to prevent irradiation damage (Wang et al., 2009). Data processing was done by fitting peaks of spectra from which the background was removed, and the concentration of Fe^{3+} was determined following the method described by Bourdelle and co-authors (2013) and Le Guillou and co-authors (2015).

2.5. Transmission electron microscopy

Transmission electron microscopy (TEM) was performed on one FIB-thin section of the K1 sample and two different FIB-thin sections of K2. The aim was to obtain images of the samples at the nanometric scale as well as diffraction patterns of the minerals constitutive of the samples. These latter, previously investigated by STXM-XANES, were studied by TEM, in parallel beam with selected area electron diffraction (SAED) with a JEOL 2100 F equipped with a field emission gun (FEG) operating at 200 kV and in scanning transmission electron (STEM) modes with a Thermofisher TITAN Themis-300 aberration-corrected FEI TEM operating at 300 kV. EDS data were collected by a super-X detectors system with four windowless silicon drift detectors, using a probe current of 500 pA with a dwell time of 4 µs per pixel. These data were then processed using the Hyperspy software package which allow for quantitative mapping (de la Peña et al. 2017). The chemical composition of each phase is determined by considering each pixel independently. It can also be determined by considering an area of pixels representative of a mineral and then by extracting an average EDS signal. Both methods have been used. All the data are accessible in the supplementary files (Supplementary 1 and Supplementary 2).

3. Results

3.1. Characterization at the micrometer-scale

Optical micrographs of K2 and K1 samples from the DR1-A well are shown in Figure 2. Their mineralogical assemblage is close to a monzo-diorite. They reveal feldspars, olivine, pyroxene, and amphibole as the main mineral phases. They are uncolored under in-plane polarized light and grey under crossed polars. K-feldspars have perthitic textures composed of plagioclase. Polysynthetic twinning is observed in plagioclase. Amphibole is light brown under in-plane polarized light and tends to appear brown to green under crossed polars. Pyroxene is uncolored to light green under in-plane polarized light and has second order birefringence colors under crossed polars. Their orthogonal cleavages are visible. Pyroxene and amphibole are mostly clustered around the olivine throughout the rock (Figure 2A, C, D, E, and F). Olivine is uncolored to slightly yellow under in-plane polarized light and has second order birefringence colors under crossed polars (Figure 2A, B, C, D, E, and F). They are cut by a thin and light yellow to dark brown mineral forming veins (Figure 2B and D). The thickness of these veins varies from several tens of microns to a few microns. The mineral forming the veins also mimics, in some places, the olivine shape and is associated with iron oxide (Figure 2F). The mineral forming the veins is present within the olivine, as well as within minerals in contact with the olivine. At this scale, it does not appear as clearly in the felspathic matrix as in the olivine.

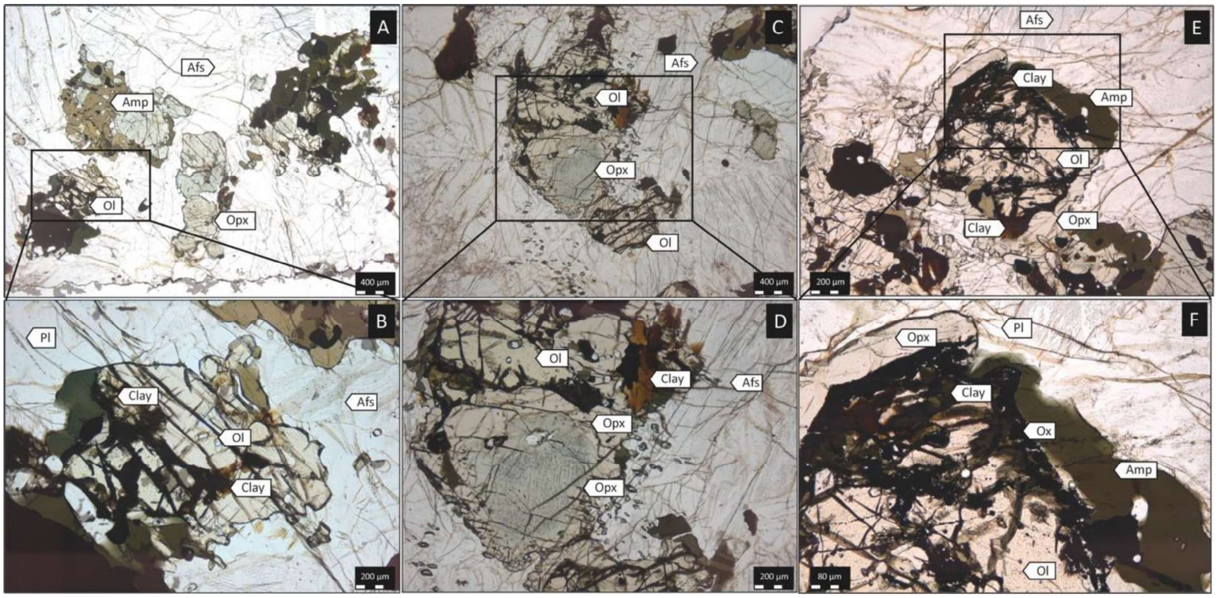

Figure 2: A- Optical micrographs in plane polarized light showing the K2 sample mineralogical assemblage; B- Optical micrographs in plane polarized light zoomed on an olivine crystal and its associated aggregates of light yellow to dark brown clay mineral seen in A; C- Optical micrograph showing K2 olivine and associated mafic minerals inside the feldspar matrix; D- Optical micrographs in plane polarized light zoomed on the olivine – orthopyroxene association seen in C; E- Optical micrographs in plane polarized light showing the K1 sample mineralogical assemblage; F- Optical micrographs in plane polarized light zoomed on the olivine and clays seen in E (Pl is for plagioclase, Afs is for K-felsdpar, Ol is for olivine, Opx is for orthopyroxene, Amp is for amphibole, Mag is for magnetite. Abbreviations have been defined by Whitney and Evans., 2010).

SEM data on K2 and K1 samples are shown in Figure 3. SEM-EDS provides semi-quantitative chemical compositions. All structural formulae given below have been recalculated from EDS data acquired with the SEM. K-feldspar is orthoclase with the following structural formula: $K_{0.8}Na_{0.2}AlSi_3O_8$. Plagioclase is albite with the following structural formula: $Na_{0.8}Ca_{0.2}Al_{1.2}Si_{2.8}O_8$. Rims of plagioclase are seen around the olivine, which is not the case for orthoclase. Both feldspars are closely associated and form perthitic textures with the albite being formed from the orthoclase.

Mafic minerals are seen as aggregates and can also form rims around olivine (Figure 3A and C). Note that plagioclase is also found at the border of these rims. These mafic rims are composed of amphibole identified as iron-rich pargasite: $Na_{0.4}Ca_{1.7}Fe_{3.5}Mg_{1.1}K_{0.2}Al_{1.9}Si_6O_{22}(OH)_2$ and orthopyroxene as ferrosilite: $Fe_{1.6}Mg_{0.5}Mn_{0.1}Si_2O_6$ (Figure 4A, B, and C). In some areas, these ferrosilites are associated with clinopyroxene identified as augite: $Ca_{0.7}FeMg_{0.3}Si_2O_6$. Together they form large exsolution textures of several hundreds of microns in length. These iron-rich minerals have crystallized around more or less well-preserved olivine. They have been identified as fayalite, the iron-rich endmember of olivine: $Fe_{1.8}Mn_{0.1}Mg_{0.1}SiO_4$. They are crosscut by veins of minerals rich in Fe and Si (Figure 3B and D).

Veins crosscutting fayalite in the K2 and K1 samples exhibit different phases, symmetrically distributed along the axes of the vein. They are made of an external part in direct contact with the fayalite. Note that veins only exhibit external parts within the fayalite. The contact between the external part of the veins and the hosting olivine is mostly characterized by scalloped patterns (Figure 4A). These veins are also made of a central part sometimes associated with iron oxide, apatite, and quartz (Figure 3B and D and Figure 4A). SEM investigations reveal that the central part of the vein is observed in the fayalite, the amphibole, the orthopyroxene, and the albite. Except for the areas containing iron oxide, apatite, and quartz, these veins are mainly composed of Si and Fe, with the internal parts exhibiting higher Fe/Si values (Fe/Si of 1.2) than the external part of the veins (Fe/Si of 0.9). Narrower veins (smaller than a micron) can also be seen within the K-feldspar mesostasis (Figure 3D and Figure 4). Their width, being under the resolution of the SEM, does not allow to conclude on their composition and similarities and/or differences with the veins within the other minerals. Patches of such Fe and Si-rich minerals are also identified within the fayalite.

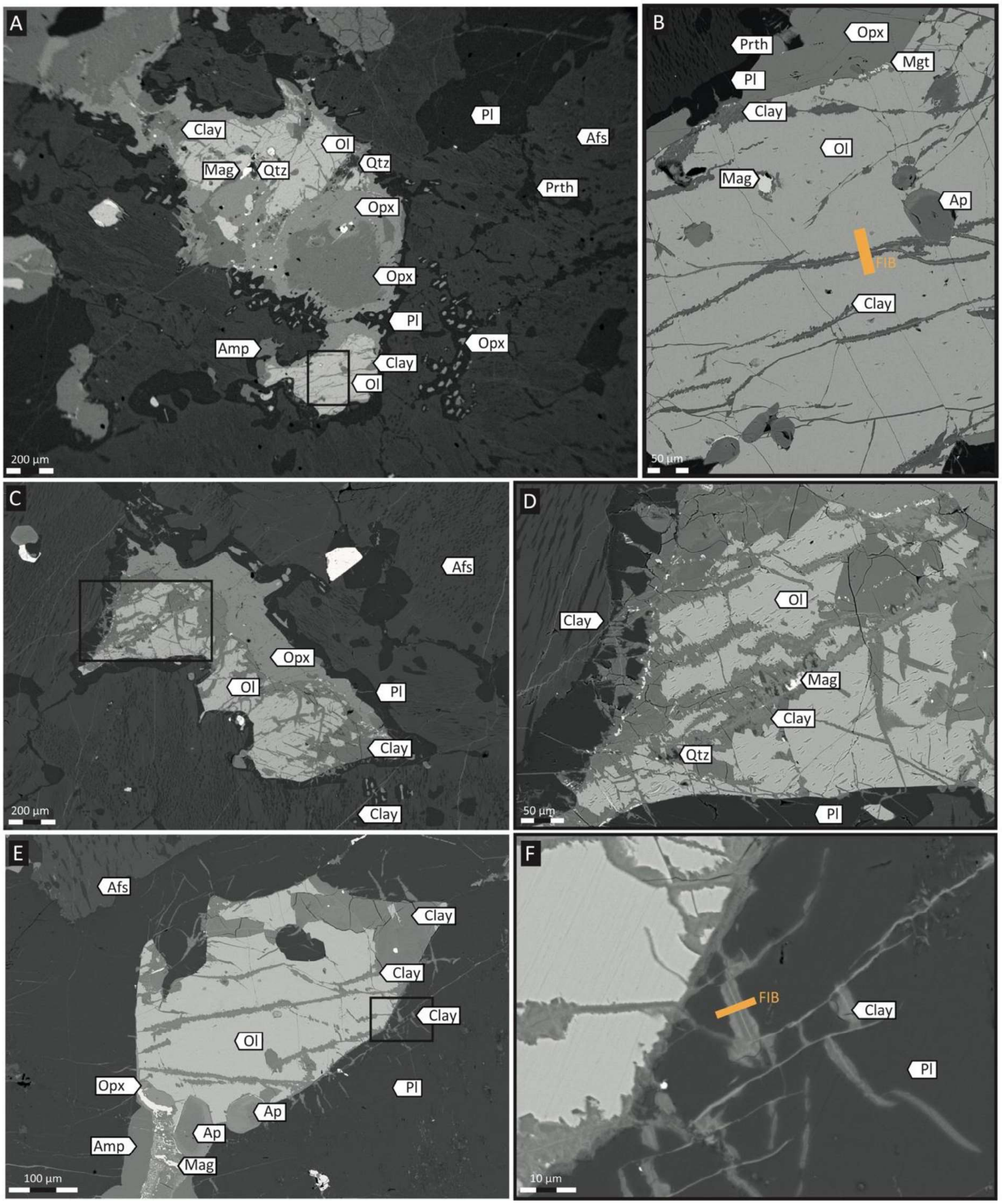

Figure 3: SEM images of A- The mineralogical assemblage of the K2 sample with an aggregate of mafic minerals; B- Veins of clay minerals going through an olivine grain, associated with apatite and iron oxide with the location of the FIB thin-section; C- The mineralogical

assemblage of K1 sample with a rim of orthopyroxene and plagioclase in a K-feldspars mesostasis; D- Veins and patches of clay minerals inside a olivine crystal, clay minerals are associated to iron oxide and quartz; E- The mineralogical assemblage in K1 with the propagation of the veins in the plagioclase; F- Zoom on the veins within the plagioclase and localization of the K1 FIB thin-section (Pl is for plagioclase, Afs is for K-feldspar, Ol is for olivine, Opx is for orthopyroxene, Amp is for amphibole, Mag is for magnetite, Ap is for apatite, Qtz is for quartz, Prth is for perthite).

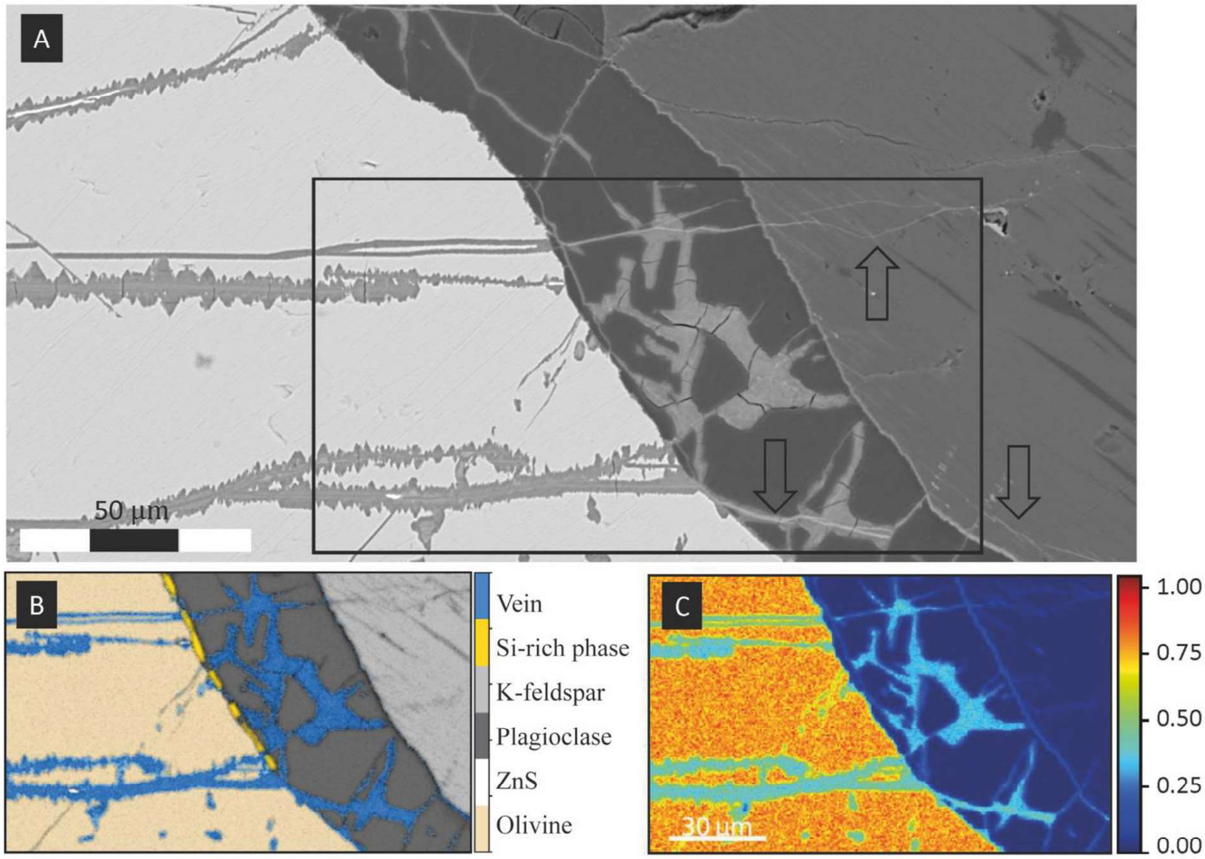

Figure 4: A- High-resolution SEM image of the olivine grain in the K2 sample and the propagation of the veins inside the rim and the mesostasis (see black arrows); B- Phase mapping (hyperspy) of the propagation of the veins; C- Mapping of the Fe/Si ratio signal, the color scale represents the ratio of the intensity of the X-ray signal, i.e., the number of counts.

Similar veins were observed in the K1 sample, showing orthopyroxenes and amphiboles in addition to quartz, iron oxides, and Fe – Si-rich minerals (Figure 5A and B). Due to the complex symplectic texture, it is difficult to assign these minerals to a specific part of the vein but what is striking is that these symplectites are limited to the fayalite and do not propagate to the other minerals. Some small iron oxides are also visible at the contact between the fayalite and orthopyroxene (Figure 5B).

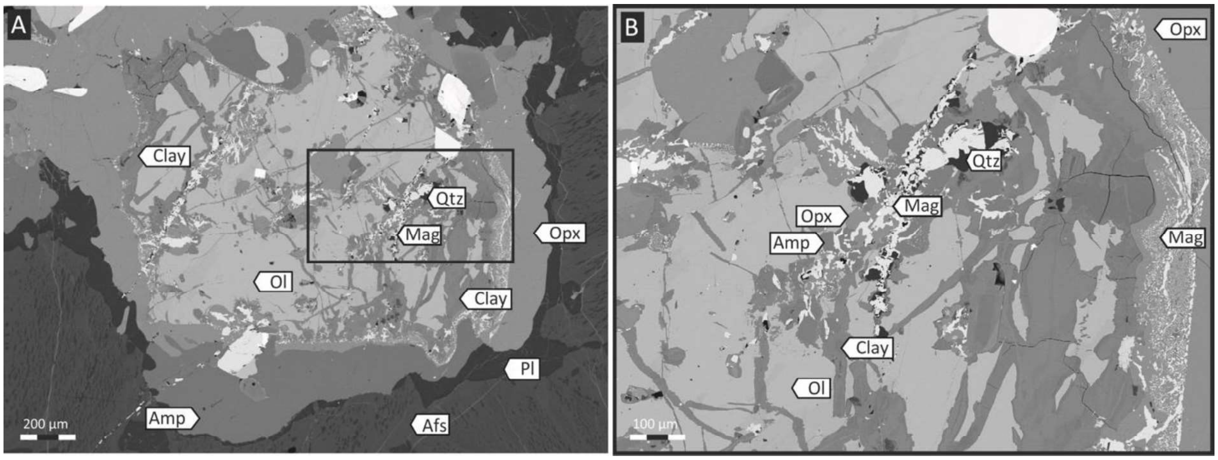

Figure 5: SEM images of the K1 sample, A- An olivine crystal with its rim of mafic minerals (Opx and Amp) and plagioclase; B- A zoom on one vein inside the olivine showing intergrowth of clay minerals, quartz, and magnetite and mafic minerals such as amphibole and orthopyroxene, at the right of the image magnetite can also be found at the border of the orthopyroxene.

Further investigations down to the nanoscale were conducted using STXM and TEM on FIB thin sections extracted from a vein hosted by a fayalite from the K2 sample and a vein hosted by a plagioclase from the K1 sample.

3.2. Characterization at the sub-micrometer-scale

The spatially resolved STXM-XANES data collected over the FIB-thin section extracted from a vein hosted by fayalite from the K2 sample (Figure 6A) reveal that the fayalite does not contain Fe^{3+} (($[Fe^{3+}]/\sum Fe=0.01\pm0.02$). In contrast, the phases composing the veins contain more than 20% of Fe^{3+}. The external part of the vein in direct contact with the fayalite is richer in Fe^{3+} ($[Fe^{3+}]/\sum Fe=0.27\pm0.02$) than the internal part ($[Fe^{3+}]/\sum Fe=0.19\pm0.02$). The internal part of the vein is also not homogeneous in terms of Fe^{3+} concentrations, with areas exhibiting ($[Fe^{3+}]/\sum Fe$) values higher than 0.2 while other areas of the internal part display values of about 0.15 (Figure 6B and C).

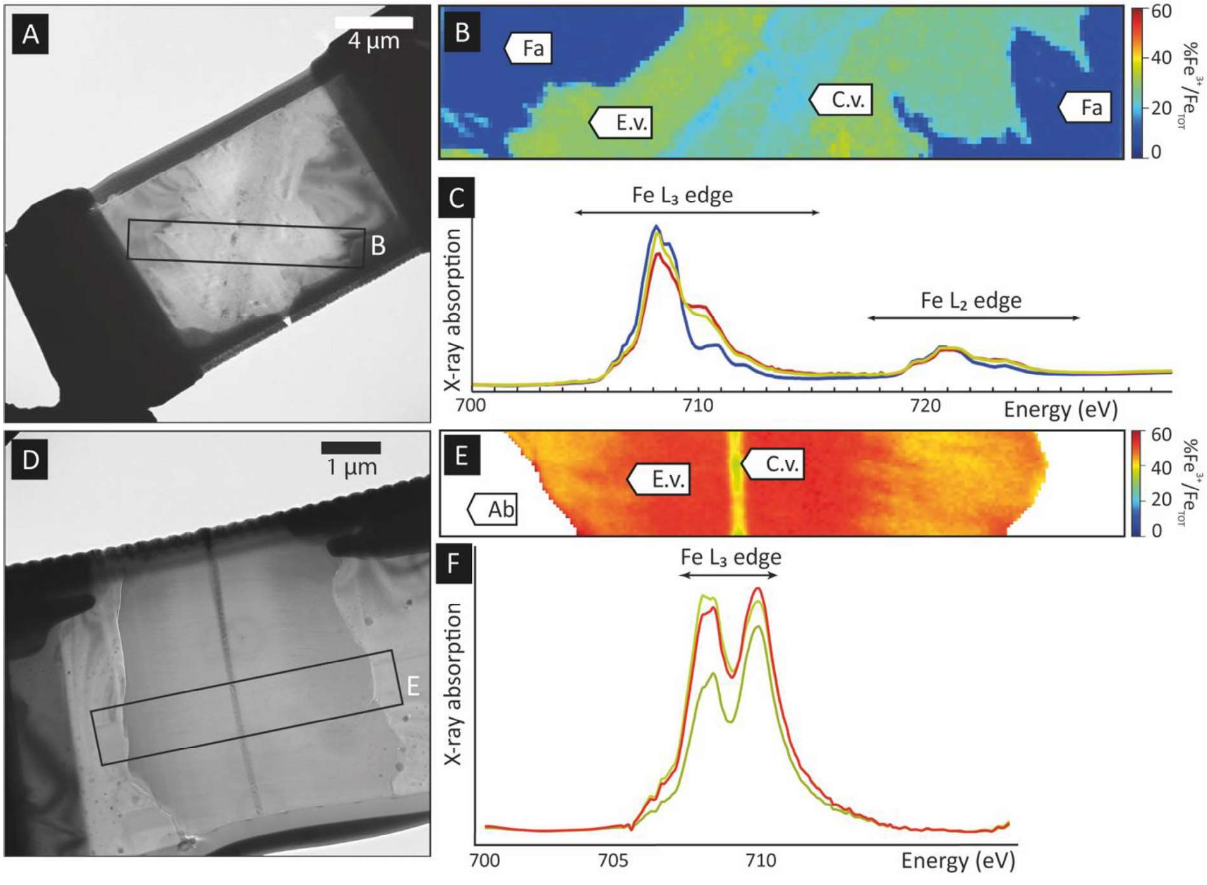

Figure 6: A- TEM image of the K2 FIB thin-section with the area mapped; B- Quantitative map of iron(III) in the K2 FIB-thin section, each pixel corresponds to the percentage of iron(III) on total iron (Fa is for fayalite, E.v. is for external vein, C.v. is for central vein); C- Global X-ray absorption spectra for each part of the FIB-thin section (blue spectra is for the fayalite, red

spectra is for the external vein and green spectra is for the central vein), D- TEM image of the K1 FIB-thin section with the area mapped; E- Quantitative map of iron(III) in the K1 FIB thin-section (Ab is for albite, E.v. is for external vein, C.v. is for central vein); F- Global X-ray absorption spectra for each part of the area mapped (light green spectra is for the center of the vein, red spectra is for the border of the vein in direct contact with the plagioclase and dark green spectra is for the part between the border and the center mineral).

Spatially resolved STXM-XANES data were also collected on the FIB-thin section extracted from a vein hosted by an albite from the K1 sample (Figure 6D). The collected data reveal that the vein is not homogeneous in Fe^{3+}, with values of about 0.40 in the very central part (Figure 6E and F) while the remaining vein shows a gradient, with values close to 0.44 in the area in direct contact with the plagioclase and increasing up to 0.51 towards the center.

Further investigations were conducted using transmission electron microscopy (TEM), revealing that the veins are mostly made of phyllosilicates. Electron diffractions (SAED), high-resolution TEM and STEM images, as well as EDXS data, were collected to identify these phases more precisely (Figure 7).

The external part of the vein appears to be composed of two different parts displaying two distinct crystalline orientations (Figure 7A and Figure 7B). The clay minerals in direct contact with the fayalite were very unstable under the beam, but SAED patterns show d spacings of $7\dot{A}$, allowing their identification as serpentine sharing crystal orientations with the fayalite (Figure 7B b1). The contact with the fayalite presents scalloped patterns typical of alteration fronts. Conversely, the clay minerals composing the more internal part of the external vein appear well crystallized and exhibit d spacings of $14\dot{A}$, suggesting these are chlorite. It also shares crystal orientation with the fayalite (Figure 7B b2). These two parts of the external vein display similar Fe/Si values of 0.9 and exhibit 0.1 and 0.15 at% of potassium and calcium (Figure 7C), pinpointing the presence of interstratified chlorite/mica or chlorite/smectite, as also suggested by the ternary diagram shown on Figure 7D.

The internal part of the vein is heterogeneous but mostly composed of phyllosilicates which do not share crystal orientations with the fayalite (Figure 7B c). Some sheets are sub-circular and exhibit d spacings of $7\dot{A}$ (Figure 7B c1). The SAED patterns correspond to a typical polycrystalline diffraction and show three well-distinguishable spots indicating d spacing of 2.5, 3.5, and $7\dot{A}$, and two more diffuse rings indicating d spacing of 2.5 and $4.5\dot{A}$, likely corresponding to the (001), (002), and $(2\bar{1}1)$ reflection of a serpentine, even though it could also correspond to chlorite. The internal part of the vein exhibits Fe/Si values of 1.2 and lower contents of Ca and K than the external part of the vein. As the external vein, the internal vein likely contains a mixture of possibly interstratified chlorite/smectite/mica and serpentine, as also suggested by the ternary diagram shown in Figure 7D. Unlike the contact between the external part of the vein and the fayalite, the contact between the internal and the external parts of the vein is sharp.

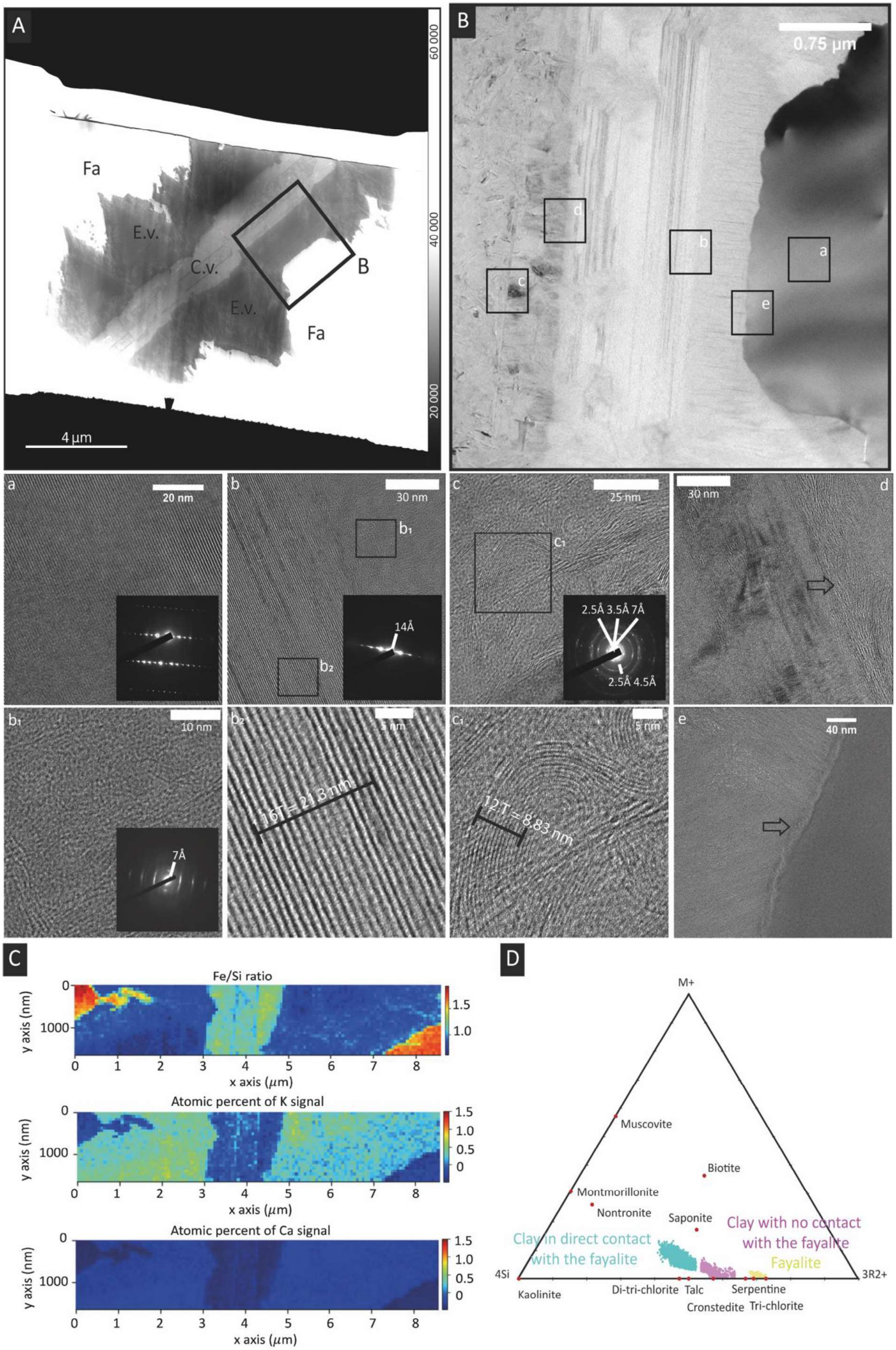
A
Fa
E.v.
C.v.
E.v.
Fa
B
4 µm
60 000
40 000
20 000
B
0.75 µm
a
b
c
d
e
a
20 nm
b
30 nm
b₁
b₂
14Å
c
25 nm
c₁
2.5Å 3.5Å 7Å
2.5Å 4.5Å
d
30 nm
b₁
10 nm
7Å
b₂
5 nm
16T = 21.3 nm
c₁
5 nm
12T = 8.83 nm
e
40 nm
C
Fe/Si ratio
Atomic percent of K signal
Atomic percent of Ca signal
y axis (nm)
x axis (µm)
0
1000
0 1 2 3 4 5 6 7 8
1.5
1.0
0.5
0
D
M+
4Si
3R2+
Muscovite
Biotite
Montmorillonite
Nontronite
Saponite
Kaolinite
Di-tri-chlorite
Talc
Cronstedite
Serpentine
Tri-chlorite
Clay in direct contact with the fayalite
Clay with no contact with the fayalite
Fayalite

Figure 7: A- STEM image of the K2 FIB thin-section showing the multiple veins inside the fayalite. The black square is for the localization of the TEM image in B (Fa is for fayalite, C.v. is for central vein and E.v. is for external vein); B- TEM image of the filling of the vein with multiple zooms on areas of interest; a- TEM high-resolution image of the fayalite and its associated electron diffraction; b- TEM high-resolution image of the clay mineral having a direct contact with the fayalite, its associated electron diffraction, and location of zooms b1 and b2 on the clay sheets; b1- Zoom on the clay mineral in direct contact with the fayalite; b2- Zoom on the well-crystallized sheets of the clay mineral in contact with the fayalite; c- TEM high-resolution image of the clay mineral with no direct contact with the fayalite and its associated electron diffraction and location of zoom c1; c1- Zoom on the sheets of the central clay mineral; d- TEM image of the contact between the two clay minerals; e- TEM image of the contact between the fayalite and the clay mineral; C- STEM-EDS maps of the Fe/Si ratio, atomic percent of K, and atomic percent of Ca of the clays going through the olivine; D- (M+; 4Si; 3R2+) ternary diagram representing the endmembers of clay minerals and the studied clay minerals in function of M+, the interlayer cationic charge as Ca or Na cations, 3R2+, the number of divalent cations in octahedral position as Fe or Mg cations and 4Si, the amount of silica. It highlights the mixing of the phases between the chlorite, the smectite, and the serpentine endmembers.

TEM investigations reveal that the architecture of the vein varies between the ones hosted by the olivine and the one hosted by the plagioclase. The vein hosted by the plagioclase only consists of the central part of the ones found in the olivine. The border part identified in direct contact with the olivine is not found in the plagioclase. Also, the vein hosted by the feldspar does not show any alteration features at the contact with the host mineral (Figure 8). Figure 8B shows a TEM image of the straight contact between the clay mineral and the plagioclase with a typical SAED pattern for the plagioclase. The SAED pattern of the vein exhibits two sets of distinguishable hexagonal spots indicating distances of 2.6 and $4.6\dot{A}$, matching with the $(\bar{1}11)$, $(1\bar{1}1)$, (020) and $(\bar{1}31)$, $(\bar{1}\bar{3}1)$, (200) reflection of a clinochlore or a mica. Figure 8C C1 shows that crystallite expands over the very central part to the rest of the vein, highlighting that this very central part is made of the same phyllosilicates. These phyllosilicates exhibit variable orientations in the very central part of the vein (Figure 8C C1) but appear perpendicular to the contact with the plagioclase (Figure 8D). In addition, STEM-EDS maps reveal Fe/Si values from 1.0 for the main part of the vein to 1.2 for the very central part (Figure 8E). Gradients in potassium and calcium maps are visible from the border to the center, with high values at the border and in the very central part. The ternary diagram, Figure 8F, shows a gradual evolution of the composition of the clay minerals from the serpentine to the micas, passing by the chlorite endmembers. It highlights that this vein, within the plagioclase, is a complex mixing of phases.

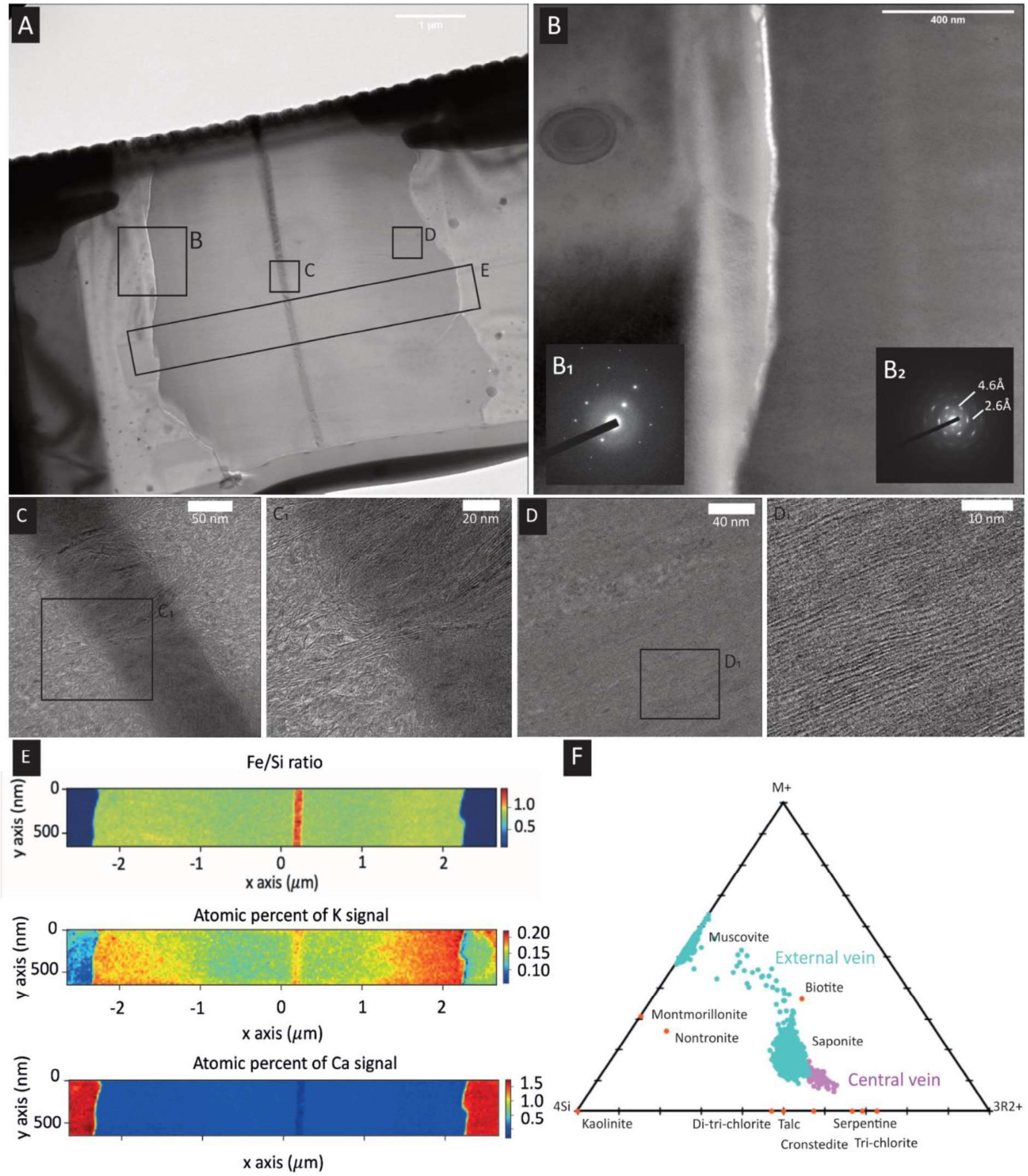

Figure 8: A- TEM image of K1 FIB thin-section; B- TEM image of the contact between the plagioclase and the vein; b1- the electron diffraction of the plagioclase; b2- The electron diffraction of the mineral filling the vein; C- HRTEM image of the center of the vein; C1- Zoom on the layers of the clay mineral filling the vein; D- HRTEM image of the border of the vein, D1- Zoom on the layers of the clay mineral that are in contact with the plagioclase; E- STEM-EDS maps of the Fe/Si ratio, the K and Ca contents (in atomic percent); F- (M+; 4Si; 3R2+)

ternary diagram representing the endmembers of clay minerals and the studied clay minerals in function of M+, the interlayer cationic charge, 3R2+, the number of divalent cations in octahedral position and 4Si, the amount of silica. It highlights the mixing of the phases between the serpentine, the chlorite, and the micas endmembers.

4. Discussion

Previous studies and drilling reports concluded that in the Nemaha County, where the DR1-A well was drilled, the Precambrian basement was composed of granite, rhyolite, and metasediments (Bickford and al., 1981; Newell et al., 2007). The drilling report from 1999 described the part of the basement reached by the well as "*a mafic-rich and dark granite with little or no quartz*". The present study concluded that the basement is closer to a monzo-diorite. K1 and K2 samples contain mafic minerals such as fayalite, iron-rich pargasite, ferrosilite, and augite dispersed within an albite and orthoclase mesostasis which does not contain any crystal of quartz. Mafic minerals have crystallized in aggregates and have a rim of albite. Pyroxene, located in contact with the fayalite, displays exsolution textures. The rest of the sample is composed of orthoclase with perthitic textures. These textures indicate K-feldspars and pyroxenes that have undergone a sub-solidus re-equilibration (Harlov et al., 1998, Putnis et al., 2007). This type of sub-solidus evolution is typical of plutonic rocks which undergo more or less slow cooling or have enough water, chlorine, and/or fluorine to have a sufficiently low enough solidus. Indeed, water, chlorine, and fluorine induce changes in the properties of the magma (Filiberto and Treiman, 2009 a & b, Dalou et al., 2015). Altogether, the rock composing the Precambrian basement in that area has been produced following a classical sequence of crystallization with fayalite crystallizing first, followed by pyroxene, iron-rich pargasite, albite, and then orthoclase. The whole-rock analysis shown in the supplementary material (Supplementary 3) confirms that this rock is a monzo-diorite. Thus, the Precambrian basement reached by the DR1-A well at the depth of 442 and 450 meters is not a Precambrian granite, as previously reported. Although that well is located around 100 km east of the axis of the Mid-Continent rift, we suggest that it reached an eastern and so-far unmapped extension of the rift.

A main observation of the present study is the occurrence of veins crosscutting the fayalite and the albite/orthoclase mesostasis in all the investigated samples. The internal part of the veins is present within all the other minerals and is associated with magnetite, apatite, and quartz, while the external part is only observed within the fayalite. While they present differences at the nanoscale, these veins have similarities with iddingsite, a mixture of hydrous silicates of iron(III) previously described in several publications (Ross, 1925; Edwards, 1938; Baker, 1967; Eggleton, 1984; Smith, 1987). Iddingsite mineralogical definition and conditions of formation have been debated over the last decades (see references above). It has been described as a light yellow to reddish brown mineral (Ross, 1925) and it is associated with both non-altered augite and feldspars (Ross, 1925 and Baker, 1967). Baker (1967) has shown that iddingsite is found in fracture inside the olivine, and that its formation allows for preserving the shape of olivine. Two hypotheses of formation have been formulated: 1) deuteric alteration of olivine by a residual magmatic liquid at high temperature; 2) post-deuteric (i.e., hydrothermal) alteration of olivine at intermediate to low-temperature conditions (compared to magmatic temperatures).

Deuteric alteration has been proposed by Ross (1925) and Edwards (1938) and described as the result of interactions between a residual magmatic liquid and previously formed minerals, resulting in the metasomatism replacement of olivine by iddingsite. Authors inferred that this process happened at the end of the cooling sequence, in the presence of a residual differentiated magma rich in water (and magmatic gas) responsible for iron oxidation (Edwards, 1938). In contrast, post-deuteric (i.e., hydrothermal) alteration was proposed as the source of iddingsite by Baker (1967), Eggleton (1984), and Smith (1987). Such intermediate to low-temperature alteration of olivine by an external oxidizing fluid circulating throughout the rock may lead to the formation of more or less interstratified chlorite, smectite, and goethite (Baker, 1967, Eggleton, 1984). Interstratification seems to be controlled by the temperature, with high to intermediate temperature giving chlorite and then decreasing temperature giving a mix of chlorite, smectite, and then goethite. The temperature of formation is easily constrained because goethite is only stable under 140°C (Eggleton et al., 1984). It seems more complicated to constrain chlorite formation as its range of formation goes from magmatic temperature (Viennet et al., 2020, 2021) to several hundred degrees (Baker, 1967). In this iddingsite definition, the system is marked by a loss of silica and magnesium, but a preservation of manganese, and iron, this latter being oxidized.

Here, the most likely scenario for the formation of iddingsite veins involves deuteric alteration (Figure 9). The internal part of the veins could have been produced via the direct precipitation of a late, differentiated magmatic fluid having been exsolved during the crystallization of the K-feldspars as perthites. The internal part of the veins is, indeed, composed of interstratified chlorite/smectite/mica mixed with serpentine, iron-oxide, apatite, and quartz (Figure 9B), which are mineral phases typical of what could produce a residual, differentiated magma close to a granitic composition (De Pasquale and Jenkins, 2023).

Here, such residual magma liquid, likely obtained during the crystallization of K-feldspars, has penetrated within the fractures or voids within the previously formed mafic minerals and plagioclase. This magmatic fluid being chemically far from equilibrium with the fayalite, was responsible for deuteric alteration of this latter, producing the external parts of the veins (Figure 9C). The first phase replacing the fayalite must have been the interstratified chlorite-smectite. At some point, with the decreasing temperature, the alteration of the fayalite led to the production of serpentine (Figure 10D). Such production of Fe-rich clay minerals via the deuteric alteration of fayalite is supported by the recent study of De Pasquale and Jenkins (2023), having shown that a mixture of fayalite and more differentiated phases such as iron oxide, albite, quartz, and magnetite exposed to a decreasing temperature in the presence of water leads to the production of Fe-rich smectite.

Of note, the clay minerals composing the internal vein hosted by the fayalite and the veins hosted by the albite exhibit spatially variable Fe contents and $[Fe^{3+}]/\sum Fe$ values. Similar variations have been described by Meunier et al. (2008, 2012) for masses of magmatic Fe-rich saponite and chlorite found in basalts from the Mururoa Atoll (French Polynesia). These authors interpreted the Fe-zoning of these clay minerals, which crystallized at the end of the cooling stage of the basaltic bodies, as resulting from variations of iron availability in the residual magmatic fluid. Indeed, the authors propose that during the cooling stage, the composition of the magma changes with increasing crystallization ratio so that the composition of the residual magmatic liquid yielding the clay minerals varies. In addition, during the crystallization of the residual liquid, some elements are depleted because they are solubilized or because they are consumed by the crystallizing minerals, leading to the zoning observed. A similar explanation can be proposed here to explain the observed variations in Fe/Si values and $[Fe^{3+}]/\sum Fe$ values within the same veins.

An alternative scenario may involve external fluids having circulated within the monzo-diorite. Surface cold waters are usually undersaturated with respect to feldspars, which means that plagioclase and alkali feldspar may undergo weathering processes occurring at low temperature (Plümper and Putnis., 2009). Such processes may lead to mineral replacement, which will result in the production of new phases such as sericite or epidote exhibiting sharp mineral interfaces and a higher porosity (Plumper and Putnis., 2009). This is not the case here, which suggests that the rocks investigated did not experience fluid circulation at low temperature. However, it is commonly acknowledged that hydrothermal waters above 200°C are close from equilibrium with plagioclase and alkali feldspar, which means that such fluids will not alter these mineral species (Stefánsson and Arnórsson., 2000). Thus, a late circulation of external fluids at rather high temperature cannot be excluded based on the mineral assemblage described here. The chemical composition of such a fluid would have to be close to that of a residual magmatic fluid to allow for such a precipitation of chlorite, smectite, and mica interstratified at the nanoscale (Mas et al., 2008).

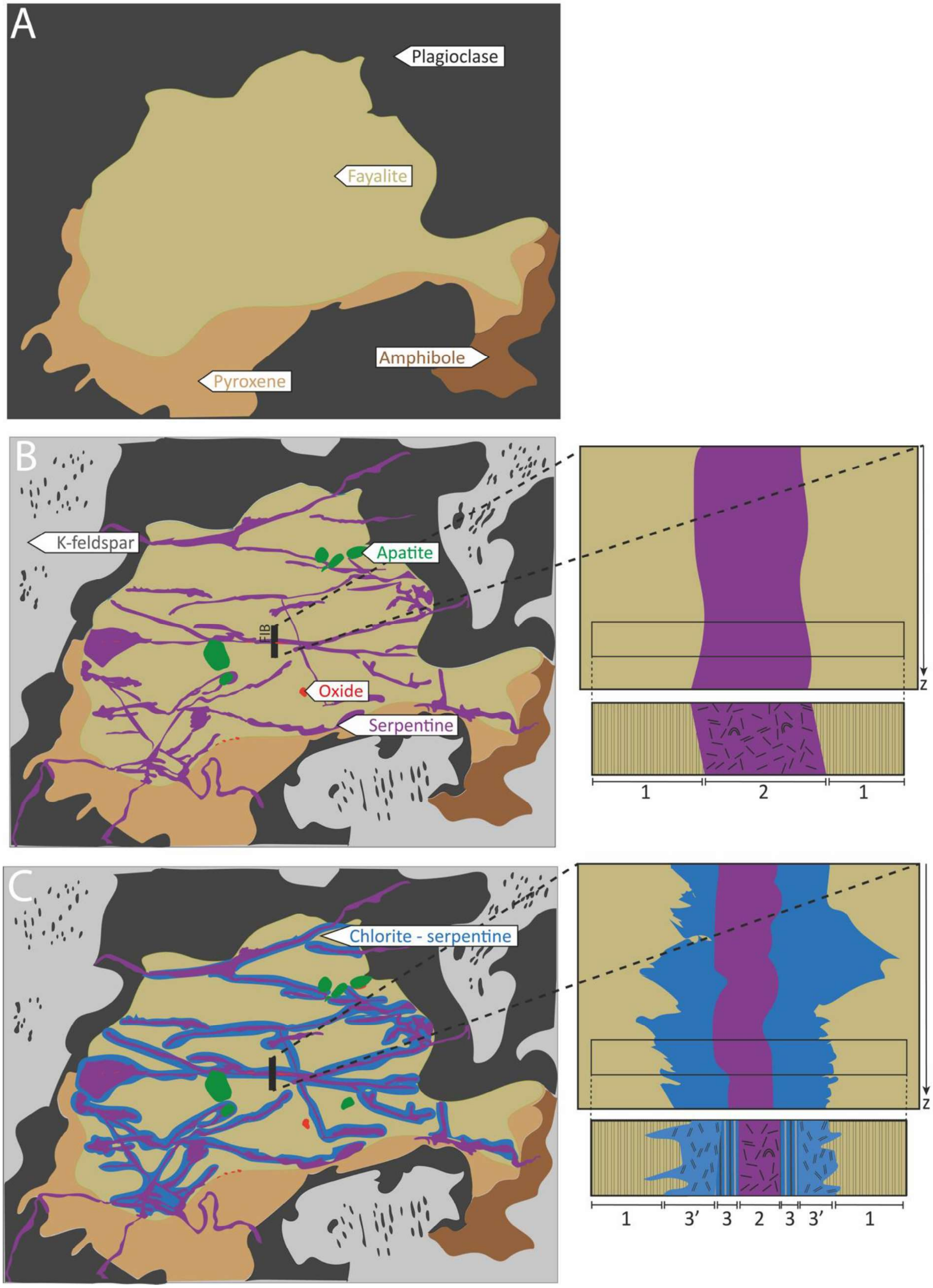

Figure 9: Synthesis sketches of the crystallization sequence in the K1 and K2 samples and zooms on veins formation; A- Fayalite, pyroxene, amphibole, and plagioclase in rims around

the mafic minerals; B- Circulation of a differentiated residual magmatic liquid which give perthitic K-feldspars and leads to the crystallization of the center chlorite/smectite/mica mixed with serpentine and the exsolution of water. Apatite and iron oxides also crystallize at that time. The mixture of minerals is crosscutting every previous mineral. Associated are zoom and sketches of the filling of the vein (1 is for the crystallization of the fayalite and 2 for the crystallization of the chlorite/smectite/mica mixed with serpentine); C- Deuteric alteration of the fayalite by the exsolved water leading to the crystallization of the interstratified chlorite-smectite and then of the serpentine in direct contact with the fayalite while the temperature is decreasing. These two clay minerals are only found in fayalite. Associated are zoom and sketches of the filling of the vein (1 is for the crystallization of the fayalite, 2 for the crystallization of the chlorite/smectite/mica mixed with serpentine, 3 for the crystallization of the interstratified chlorite-smectite, and 3' for the crystallization of the serpentine of the border vein).

5. Conclusions and implications for H_2 production

The monzo-diorites investigated here which have been described as the source of H_2 emissions contain veins of Fe-rich clay minerals, composed of a nanoscale mixture of chlorite, smectite, mica, and serpentine, likely produced via the direct precipitation of a late, differentiated magmatic fluid. Because this magmatic fluid was chemically far from equilibrium with the fayalite, it has been responsible for its deuteric alteration, producing the external parts of the veins. The crystallization begun with the fayalite being replaced by the interstratified chlorite-smectite. While the temperature was decreasing, the crystallization process ended with fayalite being replaced by serpentine via deuteric alteration.

The deuteric alteration of olivine being an oxidative process (Ross., 1925; Edwards., 1938), the production of the external part of the veins hosted by the fayalite via deuteric alteration may have produced the H_2 that is now measured at the surface. Alternatively, or concurrently, it can be conceived that H_2 was originally present in the magma, as reported in some systems (Fischer and Chiodini., 2015), with H_2 still present within the residual magmatic liquid from which the veins have precipitated. Both these hypotheses involve magmatic processes, implying that the generation of H_2 occurred during the formation of the rock, i.e., not recently (the basement of this intracratonic area originates from the Precambrian and currently does not exceed 60°C - Newell et al., 2007). Therefore, from the material studied here, H_2 could be considered partly as a “fossil” volatile. The measurements of H_2 during the last decades (Coveney et al., 1987; Newell et al., 2007; Guélard et al., 2017) and the petrological observations presented in this study suggest that H_2 has been stored in these rocks in some way, either as fluid inclusions or within the structure of the minerals. Malaspina and co-authors (2023) have recently demonstrated that molecular H_2 could be stored in inclusions within olivine under high pressure conditions, while Truche and co-authors (2018) have demonstrated that H_2 could be stored in nanopores of chlorites thanks to adsorption mechanisms. This could be the case here, potentially making the clay minerals studied here the reservoir of H_2 if not both the source and the reservoir.

Despite all these observations and conclusions, it is essential to mention that H_2 generation at the well head in Kansas was shown to be a regional trend and to be characterized by a continuous flux of gas by Guélard and co-authors (2017). We therefore cannot exclude that, other processes, such as current and low-temperature oxidation of iron, could take place in other rocks of the basement (not reached by the DR1-A well). Thus, part of H_2 generation and migration could still be a contemporaneous and active process. Furthermore, iron oxidation reactions occurring within the 350 meters of Paleozoic sedimentary rocks are also not to be excluded. We propose here a first scenario of H_2 generation linked to a late magmatic event.

However, since H_2 is currently produced at the surface and is characterized by a regional flux, it remains possible that this gas is the product of multiple reactions.

Appendix A. Supplementary Material

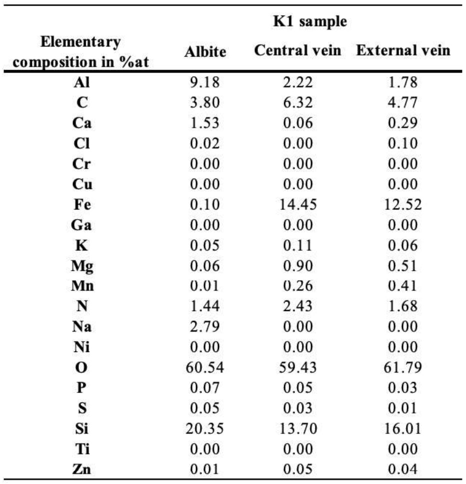

Elementary composition in %at	Albite	K1 sample Central vein	External vein
Al	9.18	2.22	1.78
C	3.80	6.32	4.77
Ca	1.53	0.06	0.29
Cl	0.02	0.00	0.10
Cr	0.00	0.00	0.00
Cu	0.00	0.00	0.00
Fe	0.10	14.45	12.52
Ga	0.00	0.00	0.00
K	0.05	0.11	0.06
Mg	0.06	0.90	0.51
Mn	0.01	0.26	0.41
N	1.44	2.43	1.68
Na	2.79	0.00	0.00
Ni	0.00	0.00	0.00
O	60.54	59.43	61.79
P	0.07	0.05	0.03
S	0.05	0.03	0.01
Si	20.35	13.70	16.01
Ti	0.00	0.00	0.00
Zn	0.01	0.05	0.04

Supplementary 1 : Mean elemental composition of the phases of the FIB thin section of K1 (data have been acquired by TEM analysis and are in atomic percent)

Please see the Excel files attached.

Supplementary 2 : Full elemental composition of the FIB thin section of K2 (data have been acquired by TEM analysis and are in atomic percent)

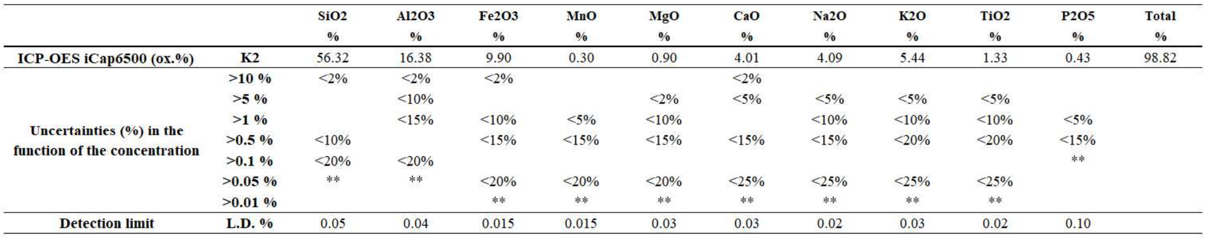

		SiO2 %	Al2O3 %	Fe2O3 %	MnO %	MgO %	CaO %	Na2O %	K2O %	TiO2 %	P2O5 %	Total %
ICP-OES iCap6500 (ox.%)	**K2**	56.32	16.38	9.90	0.30	0.90	4.01	4.09	5.44	1.33	0.43	98.82
Uncertainties (%) in the function of the concentration	**>10 %**	<2%	<2%	<2%			<2%					
	>5 %		<10%			<2%	<5%	<5%	<5%	<5%		
	>1 %		<15%	<10%	<5%	<10%		<10%	<10%	<10%	<5%	
	>0.5 %	<10%		<15%	<15%	<15%	<15%	<15%	<20%	<20%	<15%	
	>0.1 %	<20%	<20%								**	
	>0.05 %	**	**	<20%	<20%	<20%	<25%	<25%	<25%	<25%		
	>0.01 %			**	**	**	**	**	**	**		
Detection limit	**L.D. %**	0.05	0.04	0.015	0.015	0.03	0.03	0.02	0.03	0.02	0.10	

Supplementary 3: Whole-rock chemistry data of the K2 sample (in weight percent)

Declaration of competing interest

The authors declare that they have no known competing financial interests or personal relationships that could have appeared to influence the work reported in this paper.

Acknowledgments

This work was supported by E2S UPPA/ the Nouvelle-Aquitaine Region and by the “France 2030” Investment Program managed by the French National Research Agency (ANR-16-IDEX-0002). H. Derluyn acknowledges the support from the European Research Council (ERC) under the European Union’s Horizon 2020 research and innovation program (grant agreement No 850853)”. The authors wish to acknowledge the workforce of the SEM facility (PtME) at MNHN (Sylvain Pont) and of the TEM facility at IMPMC (Jean-Michel Guignier). Special thanks also go to David Troadec for the preparation of FIB sections at IEMN, as well as to Stefan Stanescu and Sufal Swaraj for their expert support with the HERMES STXM beamline at SOLEIL. The HERMES beamline (SOLEIL) is supported by the CNRS, the CEA, the Region Ile de France, the Departmental Council of Essonne, and the Region Centre. The TEM facility at the CCM (Lille University) is supported by the Chevreul Institute, the European FEDER, and Region Nord-Pas-de-Calais. The authors wish to acknowledge the Kansas Geological Survey and K.D. Newell for their help through sampling.

References

Baker, I., Haggerty, S.E., 1967. The alteration of olivine in basaltic and associated lavas. Contributions to Mineralogy and Petrology 16, 233–257. https://doi.org/10.1007/bf00371094

Belkhou, R., Stanescu, S., Swaraj, S., Besson, A., Ledoux, M., Hajlaoui, M., Dalle, D., 2015. HERMES: a soft X-ray beamline dedicated to X-ray microscopy. Journal of Synchrotron Radiation 22, 968–979. https://doi.org/10.1107/s1600577515007778

Bernard, S., Benzerara, K., Beyssac, O., Brown, G.E., Stamm, L.G., Duringer, P., 2009. Ultrastructural and chemical study of modern and fossil sporoderms by Scanning Transmission X-ray Microscopy (STXM). Review of Palaeobotany and Palynology 156, 248–261. https://doi.org/10.1016/j.revpalbo.2008.09.002

Bickforf, M.E., Harrower, K.L., Hoppe, W.J., Nelson, B.K., Nusbaum, R.L., Thomas, J.J., 1981. Rb-Sr and U-Pb geochronology and distribution of rock types in the Precambrian basement of Missouri and Kansas. GSA Bulletin 92, 323–341. https://doi.org/10.1130/0016-7606(1981)92%3C323:RAUGAD%3E2.0.CO;2

Bourdelle, F., Benzerara, K., Beyssac, O., Cosmidis, J., Neuville, D.R., Brown, G.E., Paineau, E., 2013. Quantification of the ferric/ferrous iron ratio in silicates by scanning transmission X-ray microscopy at the Fe L2,3 edges. Contributions to Mineralogy and Petrology 166, 423–434. https://doi.org/10.1007/s00410-013-0883-4

Brown, W.L., Parsons, I., 1988. Zoned ternary feldspars in the Klokken intrusion: exsolution microtextures and mechanisms. Contributions to Mineralogy and Petrology 98, 444–454. https://doi.org/10.1007/bf00372364

Ciobanu, C.L., Cook, N.J., Utsunomiya, S., Pring, A., Green, L., 2011. Focussed ion beam–transmission electron microscopy applications in ore mineralogy: Bridging micro- and nanoscale observations. Ore Geology Reviews 42, 6–31. https://doi.org/10.1016/j.oregeorev.2011.06.012

Coveney, J., Goebel, E.D., Zeller, E.J., Dreschhoff, G. a. M., Angino, E.E., 1987. Serpentinization and the origin of hydrogen gas in Kansas. Am. Assoc. Pet. Geol., Bull.; (United States) 71:1.

Dalou, C., Le Losq, C., Mysen, B.O., Cody, G.D., 2015. Solubility and solution mechanisms of chlorine and fluorine in aluminosilicate melts at high pressure and high temperature. American Mineralogist 100, 2272–2283. https://doi.org/10.2138/am-2015-5201

de la Pena, F., Ostasevicius, T., Tonaas Fauske, V., Burdet, P., Jokubauskas, P., Nord, M., Sarahan, M., Prestat, E., Johnstone, D.N., Taillon, J., Caron, J., Furnival, T., MacArthur, K.E., Eljarrat, A., Mazzucco, S., Migunov, V., Aarholt, T., Walls, M., Winkler, F., Donval, G., 2017. Electron Microscopy (Big and Small) Data Analysis With the Open Source Software Package HyperSpy. Microscopy and Microanalysis 23, 214–215. https://doi.org/10.1017/s1431927617001751

Di Pasquale, B.M., Jenkins, D.M., 2022. The upper-thermal stability of an iron-rich smectite: Implications for smectite formation on Mars. Icarus 374, 114816. https://doi.org/10.1016/j.icarus.2021.114816

Edwards, A.B., 1938. The Formation of Iddingsite. American Mineralogist 23, 277–281.

Eggleton, R.A., 1984. Formation of Iddingsite Rims on Olivine: A Transmission Electron Microscope Study. Clays and Clay Minerals 32, 1–11. https://doi.org/10.1346/ccmn.1984.0320101

Filiberto, J., Treiman, A.H., 2009a. Martian magmas contained abundant chlorine, but little water. Geology 37, 1087–1090. https://doi.org/10.1130/g30488a.1

Filiberto, J., Treiman, A.H., 2009b. The effect of chlorine on the liquidus of basalt: First results and implications for basalt genesis on Mars and Earth. Chemical Geology 263, 60–68. https://doi.org/10.1016/j.chemgeo.2008.08.025

Guélard, J., Beaumont, V., Rouchon, V., Guyot, F., Pillot, D., Jézéquel, D., Ader, M., Newell, K.D., Deville, E., 2017a. Natural H2in Kansas: Deep or shallow origin? Geochemistry, Geophysics, Geosystems 18, 1841–1865. https://doi.org/10.1002/2016gc006544

Guélard, J., Beaumont, V., Rouchon, V., Guyot, F., Pillot, D., Jézéquel, D., Ader, M., Newell, K.D., Deville, E., 2017b. Natural H2in Kansas: Deep or shallow origin? Geochemistry, Geophysics, Geosystems 18, 1841–1865. https://doi.org/10.1002/2016gc006544

GuélardJ., 2016. Caractérisation des émanations de dihydrogène naturel en contexte intracratonique : exemple d’une interaction gaz/eau/roche au Kansas. theses.hal.science.

Harlov, D.E., Hansen, E.C., Bigler, C., 1998. Petrologic evidence for K-feldspar metasomatism in granulite facies rocks. Chemical Geology 151, 373–386. https://doi.org/10.1016/S0009-2541(98)00090-4

Le Guillou, C., Brearley, A., 2014. Relationships between organics, water and early stages of aqueous alteration in the pristine CR3.0 chondrite MET 00426. Geochimica et Cosmochimica Acta 131, 344–367. https://doi.org/10.1016/j.gca.2013.10.024

Mas, A., Meunier, A., Beaufort, D., Patrier, P., Dudoignon, P., 2008. Clay minerals in basalt-hawaiite rocks from Mururoa Atoll (French Polynesia). I. Mineralogy. Clays and clay minerals 56, 711–729. https://doi.org/10.1346/ccmn.2008.0560611

Merriam, D.F., 1963. The geologic history of Kansas. Proceedings of the United States National Museum.

Meunier, A., Mas, A., Beaufort, D., Patrier, P., Dudoignon, P., 2008. Clay minerals in basalt-hawaiite rocks from Mururoa Atoll (French Polynesia). II. Petrography and geochemistry. Clays and clay minerals 56, 730–750. https://doi.org/10.1346/ccmn.2008.0560612

Newell, K.D., Doveton, J.H., Merriam, D.F., Lollar, B.S., Waggoner, W.M., Magnuson, L.M., 2007. H2-rich and Hydrocarbon Gas Recovered in a Deep Precambrian Well in Northeastern Kansas. Natural Resources Research 16, 277–292. https://doi.org/10.1007/s11053-007-9052-7

Plümper, O., Putnis, A., 2009. The Complex Hydrothermal History of Granitic Rocks: Multiple Feldspar Replacement Reactions under Subsolidus Conditions. Journal of Petrology 50, 967–987. https://doi.org/10.1093/petrology/egp028

Putnis, A., Hinrichs, R., Putnis, C.V., Golla-Schindler, U., Collins, L.G., 2007. Hematite in porous red-clouded feldspars: Evidence of large-scale crustal fluid–rock interaction. Lithos 95, 10–18. https://doi.org/10.1016/j.lithos.2006.07.004

Ross, C.S., Shannon, E.V., 1925. The origin, occurrence, composition, and physical properties of the mineral iddingsite.

Smith, K.L., 1987. Weathering of Basalt: Formation of Iddingsite. Clays and Clay Minerals 35, 418–428. https://doi.org/10.1346/ccmn.1987.0350602

Steeples, D.W., DuBois, S.M., Wilson, F.W., 1979. Seismicity, faulting, and geophysical anomalies in Nemaha County, Kansas: Relationship to regional structures. Geology 7, 134–138. https://doi.org/10.1130/0091-7613(1979)7%3C134:SFAGAI%3E2.0.CO;2

Stefánsson, A., Arnórsson, S., 2000. Feldspar saturation state in natural waters. Geochimica et Cosmochimica Acta 64, 2567–2584. https://doi.org/10.1016/s0016-7037(00)00392-6

Swaraj, S., Belkou, R., Stanescu, S., Rioult, M., Besson, A., Hitchcock, A.P., 2017. Journal of Physics: Conference Series [WWW Document].

Truche, L., Joubert, G., Dargent, M., Martz, P., Cathelineau, M., Rigaudier, T., Quirt, D., 2018. Clay minerals trap hydrogen in the Earth's crust: Evidence from the Cigar Lake uranium deposit, Athabasca. Earth and Planetary Science Letters 493, 186–197. https://doi.org/10.1016/j.epsl.2018.04.038

Viennet, J.-C. ., Bernard, S., Le Guillou, C., Sautter, V., Schmitt-Kopplin, P., Beyssac, O., Pont, S., Zanda, B., Hewins, R., Remusat, L., 2020. Tardi-magmatic precipitation of Martian Fe/Mg-rich clay minerals via igneous differentiation. Geochemical Perspectives Letters 47–52. https://doi.org/10.7185/geochemlet.2023

Viennet, J.-C., Bernard, S., Le Guillou, C., Sautter, V., Grégoire, B., Jambon, A., Pont, S., Beyssac, O., Zanda, B., Hewins, R., Remusat, L., 2021. Martian Magmatic Clay Minerals Forming Vesicles: Perfect Niches for Emerging Life? Astrobiology 21, 605–612. https://doi.org/10.1089/ast.2020.2345

Wang, J., Morin, C., Li, L., Hitchcock, A.P., Scholl, A., Doran, A., 2009. Radiation damage in soft X-ray microscopy. Journal of Electron Spectroscopy and Related Phenomena 170, 25–36. https://doi.org/10.1016/j.elspec.2008.01.002

Whitney, D.L., Evans, B.W., 2009. Abbreviations for names of rock-forming minerals. American Mineralogist 95, 185–187. https://doi.org/10.2138/am.2010.3371

Wirth, R., 2009. Focused Ion Beam (FIB) combined with SEM and TEM: Advanced analytical tools for studies of chemical composition, microstructure and crystal structure in geomaterials on a nanometre scale. Chemical Geology 261, 217–229. https://doi.org/10.1016/j.chemgeo.2008.05.019

Woelk, T.S., Hinze, W.J., 1991. Model of the midcontinent rift system in northeastern Kansas. Geology 19, 277–280. https://doi.org/10.1130/0091-7613(1991)019%3C0277:MOTMRS%3E2.3.CO;2